

ORIGINAL RESEARCH

Optimising collection geometry for long-range synthetic aperture sonar interferometry

Roy Edgar Hansen^{1,2}  | Torstein Olsmo Sæbø¹ ¹Norwegian Defence Research Establishment (FFI), Kjeller, Norway²Department of Informatics, University of Oslo, Oslo, Norway**Correspondence**

Roy Edgar Hansen.

Email: roy-edgar.hansen@ffi.no**Abstract**

Interferometric synthetic aperture sonar (SAS) is a technique to image and map the seabed in very high resolution. For large area coverage rate systems with hundreds of metres swath width, the achievable performance varies significantly over the swath. The performance is a function of system, collection geometry, and seabed type. A model is suggested to optimise the collection geometry for maximising area coverage rate given certain optimisation criteria, such as observation geometry, signal-to-noise ratio, depth measurement accuracy, and coverage within swath. The model is fitted to measurements (or calibrated) through a simple procedure. Specifically, the effect of vehicle altitude during the interferometric SAS data collection is studied. A novel model on data collected by a HUGIN Superior autonomous underwater vehicle carrying a HISAS 1032 Dual Rx interferometric SAS is demonstrated. The authors show that optimising the collection geometry, and in this case specifically the vehicle altitude, significantly improves the overall performance.

KEYWORDS

radar interferometry, sonar imaging, synthetic aperture sonar

1 | INTRODUCTION

Interferometric synthetic aperture sonar (SAS) is a technique with the potential to produce very high resolution images and maps of the seabed [1]. The technique has strong similarities to interferometric synthetic aperture radar (SAR) [2, 3]. Interferometric SAS is typically carried by underwater vehicles (AUV) running at an altitude of a few tens of metres above the seabed. A common system setup consists of a separate starboard and port interferometric SAS, where there is a blind zone and a nadir gap directly below the AUV. The instantaneous area coverage rate therefore becomes the vehicle speed multiplied by two times the maximum range with the nadir gap subtracted [4].

The maximum range of a SAS system is proportional to the length of the receiver array along-track, a critical and well known design limitation [5, 6]. This imposes a clear difference between SAR and SAS systems [7, 8].

For successful interferometry processing, that is, forming seabed maps from the interferograms, the signal-to-noise ratio

(SNR) must be sufficient. This affects both the achievable depth standard deviation (STD) [9, 10] and the probability of wrap error [11, 12].

By increasing the length of the receiver array, the imaging swath increases correspondingly. However, for a given sonar frequency and sonar signal energy, the SNR may become marginal, or even too low, for accurate bathymetric mapping out to maximum range [12]. One approach is to increase the spatial averaging in the phase estimation filter [13].

In this paper, we suggest to optimise the collection geometry in order to maximise the achievable swath for selected performance criteria. Specifically, we study the choice of vehicle altitude during the interferometric SAS data collection, and how it affects the performance. This study is an extension and a direct continuation of ref. [14]. Our approach is as follows. We develop a simple model by combining scattering physics and the power budget (the sonar/radar equation). We then fit the model to the estimated SNR from interferometric coherence assuming scene homogeneity. We then use this calibrated model to calculate the

optimum vehicle altitude for a given performance criterion, either based on SNR or the theoretical interferometric depth accuracy.

We evaluate our approach on real data collected by a HUGIN Superior AUV [15] carrying a HISAS 1032 Dual Rx interferometric SAS [16] (Figure 1). We show that by optimising the collection geometry, the performance and/or the area coverage rate can be significantly improved.

In Section 2, we describe the theoretical foundations for modelling performance. Section 3 describes the experiment, the data collected, the model fitting and the results. Finally, we conclude our study in Section 4.

2 | THEORETICAL PERFORMANCE

The sonar or the radar equation describes the power budget and can be used to predict the SNR, with numerous excellent references in the sonar field [17, 18] and the radar field [19, 20]. In this paper, we study the effect of the collection geometry on a fixed system. Our goal is to use a simple model that links scattering physics through SNR calculations and thereby theoretical performance.

2.1 | The power budget

Following the approach in refs. [21, 22] and with reference to Figure 2, we simplify the linear power budget equation as follows:

$$\rho = C \frac{1}{N_0} D_t(\phi) D_r(\phi) \eta(2R) \frac{1}{R^3} \frac{1}{\cos \phi_g} \sigma^0(\phi_g) \quad (1)$$

where ρ is the SNR, N_0 is the additive noise level, ϕ is the direction of arrival relative to the interferometer, D_t and D_r are the transmitter and receiver element directivities in the vertical plane, R is slant range, η is the range dependent absorption loss, and ϕ_g is the grazing angle. σ^0 is the backscattering coefficient per unit area on the seabed. C is a constant containing the system dependent non-varying terms such as frequency, bandwidth, element sizes, transmit power and pulse length. Synthetic aperture processing only changes resolution, and not SNR for backscattering from a homogeneous patch of seabed (e.g. a distributed scatterer) in the pulse-limited case [23], [chapter 3]. This makes the SNR theoretically equivalent for sidescan sonar (SSS) processing and SAS processing when using the same data.

2.2 | Backscattering coefficient

The seabed backscattering coefficient σ^0 is strongly dependent of acoustic frequency and the grazing angle [24]. We use the model described in ref. [25], related to the more common model described in ref. [26]. The model uses the small-slope



FIGURE 1 HUGIN Superior with the HISAS 1032 Dual Rx system. Photo courtesy of Kongsberg Discovery.

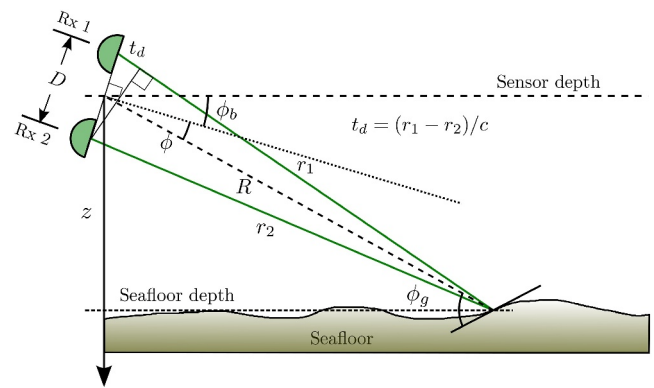


FIGURE 2 Interferometric SAS vertical geometry. R is the slant range, ϕ the direction of arrival relative to the interferometer and ϕ_g the grazing angle.

approximation for elastic roughness scattering and perturbation theory for the elastic volume scattering in the calculation of the backscattering coefficient. We have limited our study to backscattering in a single vertical plane only (2D).

Figure 3 shows the modelled backscattering coefficient for different seabed types. At small grazing angles, we see that the backscattering coefficient drops rapidly when the grazing decreases. It should be noted that the backscattering coefficient of *medium silt* is dominated by volume backscattering except near nadir $\phi_g > 80^\circ$. In this paper, the results are produced using *medium silt* or *medium sand* as the seabed type.

2.3 | Grazing angle variability

The seabed is usually not a perfectly flat surface. Seabed slope variations cause variations in ϕ_g which again cause variations in σ^0 . This results in an effective increase in the average σ^0 for very low ϕ_g . We follow [22] and model this by calculating the

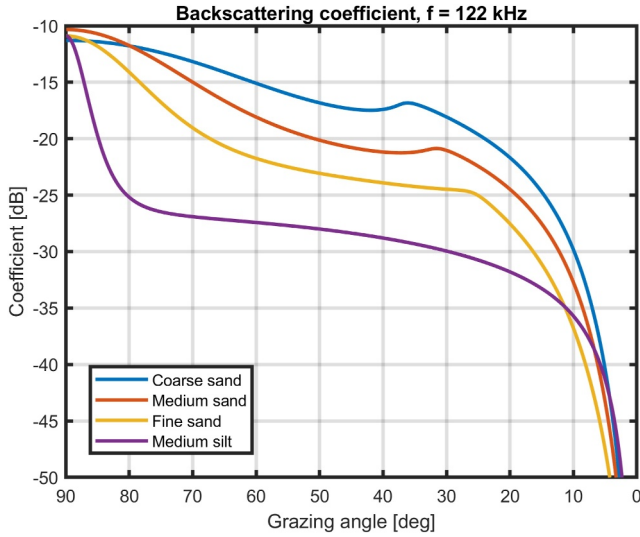


FIGURE 3 Backscattering coefficient for different seabed types for a sonar with centre frequency of 122 kHz.

average backscattering coefficient from a distribution of grazing angles around the nominal grazing angle ϕ_g given by the flat seabed

$$\sigma_r^0(\phi_g) = \int_{\phi_g - \zeta}^{\phi_g + \zeta} f_s(\phi - \phi_g) \sigma^0(\phi) d\phi \quad (2)$$

where $f_s(\phi)$ is the slope distribution given as a Gaussian distribution

$$f_s(\phi) = \frac{1}{\sqrt{2\pi}\zeta} \exp(-\phi^2/2\zeta^2) \quad (3)$$

with a width of ζ degrees. To simplify calculations, we use a modified grazing angle

$$\phi_{g,a} = \sqrt{\phi_g^2 + \zeta^2} \quad (4)$$

which gives an approximated backscattering coefficient

$$\sigma_a^0(\phi_{g,a}) \approx \sigma_r^0(\phi_g). \quad (5)$$

Figure 4 shows the backscattering coefficient for an unperturbed flat seabed (blue) compared with the average backscattering coefficient (2) (red), and the backscattering coefficient using the approximated grazing angle (4) (yellow). We have used $\zeta = 5^\circ$ which gives a reasonable fit to our real data. We see that the approximated backscattering coefficient fits well the perturbed average. Note that this correction produces a similar result as the *plateau* described in ref. [27]. In the following, we use the approximated backscattering coefficient, that is, $\phi_g = \phi_{g,a}$.

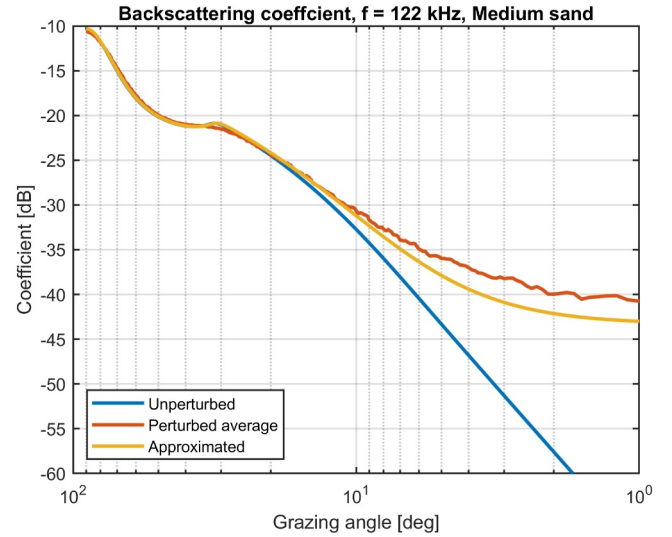


FIGURE 4 Average backscattering coefficient with slope perturbations for medium sand and a sonar with centre frequency of 122 kHz. Note that the x-axis is logarithmic.

2.4 | Interferometric accuracy

Interferometric SAS, similar to its counterpart in SAR, is the process of estimating vertical direction of arrival, ideally per horizontal resolution cell, from two or more vertically displaced SAS receiver arrays [9, 10]. Assume two receiver arrays, vertically separated with a distance D , forming an interferometer with a baseline direction ϕ_b relative to the vertical axis as illustrated in Figure 2. From the estimated time difference of arrival t_d , the direction of arrival ϕ relative to the interferometer can be calculated as follows:

$$\phi \approx \sin^{-1}\left(\frac{ct_d}{D}\right), \quad (6)$$

giving a depth of the seabed relative to the platform

$$z \approx R \sin(\phi + \phi_b), \quad (7)$$

where R is the slant range. A more detailed geometrical description can be found in ref. [10]. It should be noted that the tilt of the baseline ϕ_b only affects the interferometer, and should not be confused with the mechanical and electrical tilt of the transducers, which defines the vertical beampatterns D_t and D_r to be used in the power budget (1).

The STD of the depth estimate, or rather the theoretical lower bound, can be approximated using the Cramér–Rao lower bound (CRLB) for time delay estimation in combination with the geometry terms as follows [10, 28]:

$$\begin{aligned} \sigma_z &= \frac{R}{D} \frac{\cos(\phi_b + \phi)}{\cos \phi} c \sigma_\tau, \quad \sigma_\tau \\ &= \frac{1}{2\pi f_c} \frac{1}{\sqrt{BT}} \sqrt{\frac{1}{\rho} + \frac{1}{2\rho^2}}. \end{aligned} \quad (8)$$

BT is time-bandwidth product equal to the number of independent samples used in the time delay estimation, and ρ is the generalised SNR related to the interferometric coherence γ as follows [9, 29]:

$$\rho = \frac{\gamma}{1-\gamma}, \quad \gamma = \frac{\rho}{1+\rho} \quad (9)$$

under the assumption that uncorrelated noise is the only source for decorrelation. In this paper, we assume that additive noise is the limiting factor and the source for decorrelation at long range.

2.5 | Area coverage rate

A critical parameter in surveying an area using an AUV with SAS is the area covered per unit time, or the *area coverage rate*. Similar to sidescan sonar, there are several approaches for a two-sided sonar with a nadir gap (or blind zone) [30–32]. Consider a large rectangular area to be covered by running the vehicle in multiple parallel lines in a lawnmower pattern, and a two-sided SAS with a nadir gap. A high frequency multibeam echosounder could be used as a gap-filler [16, 33], but in this study, we build on ref. [4] and consider the *effective area coverage rate* where the SAS sensor is used to cover the entire area. Assume an AUV with velocity v , maximum one-sided ground range R_{\max} , and minimum one-sided ground range R_{\min} , given by some performance criterion. Furthermore, consider that $R_{\min} > 0$ (i. e. that there is a nadir blind-zone) and $R_{\max} \geq 3R_{\min}$ (i. e. that the one-sided swath can cover the two-sided nadir gap in a single pass). There are now multiple alternatives:

1. The entire area is covered at least from one view, and that the more area covered with two views is better. Then the area coverage rate for one view becomes

$$A = \frac{3R_{\max} - R_{\min}}{2}v. \quad (10)$$

2. Every pixel is covered with two views, one from port and one from starboard side. Then

$$A = (R_{\max} - R_{\min})v. \quad (11)$$

3. Every pixel is covered only once (minimum overlap)

$$A = 2(R_{\max} - R_{\min})v, \quad R_{\max} = 3R_{\min}. \quad (12)$$

The last alternative is illustrated in Figure 5.

If the maximum range R_{\max} can be increased at the cost of increasing R_{\min} , the most effective is the latter alternative, where the nadir blind zone is equal to the one-sided valid swath. Then, Equation (12) collapses to

$$A_{\max} = \frac{4}{3}R_{\max}v. \quad (13)$$

Note that for SAS, the along-track sampling criterion may give a hard limit to the maximum slant-range [6].

Given a performance criterion, R_{\min} and R_{\max} may be non-linear functions of altitude, making the chosen area coverage rate equation difficult to solve analytically.

3 | RESULTS

We now consider how to choose vehicle altitude in the optimisation of the collection geometry. By studying Equation (1) it is clear that the dominating effects of increasing the altitude over a flat seabed are:

1. An increased SNR at long range due to an increased grazing angle
2. A decreased SNR at short range due to the steep fall in the vertical beampattern
3. A decreased SNR at long range due to the range dependent transmission loss including the spreading loss and the absorption.

In this section, we show the measured SSS and SAS interferometric coherence, the calculated SNR, a direct technique to fit the model to the measurements, and how to optimise the collection geometry to maximise area coverage for a given desired performance criterion.

3.1 | The experiment

To verify the modelled SNR and variance of the estimated seabed depths, we use data from an experiment in February 2022, with a Kongsberg HISAS 1032 Dual Rx System [16], mounted on a HUGIN Superior AUV [15]. Each receiver array is 64 elements and 2.4 m along track, with an interferometric baseline $D = 30$ cm. The centre frequency is 122 kHz and the bandwidth is 36 kHz.

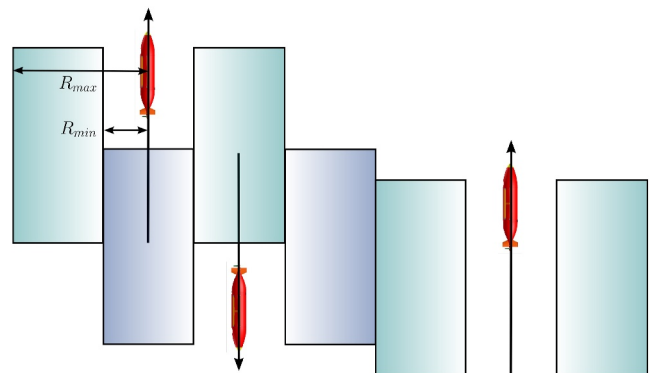


FIGURE 5 AUV track spacing for optimised coverage rate.

In the experiment, the AUV travelled six identical 4700 m tracks with different altitudes, at 200 m water depth outside Horten, Norway. All lines were run as forward and return lines, forming 12 independent data collections. The altitudes varied between the tracks, from 15 to 90 m in 15 m steps, and the recorded slant range was 370 m. All other parameters than the altitudes were fixed between the tracks.

3.2 | Measured coherence

The interferometric coherence is estimated as the magnitude of the peak normalised cross correlation coefficient between a selected patch of image pixels from the upper s_u and lower s_l array (or synthetic aperture)

$$\hat{\gamma} = \max_{\tau} \left| \frac{\langle s_l s_u^*(t - \tau) \rangle}{[\langle |s_l|^2 \rangle \langle |s_u|^2 \rangle]^{1/2}} \right|. \quad (14)$$

For SSS, we estimate the coherence per ping based on a single 1D range correlation window, and for SAS we estimate the coherence based on a 2D correlation window. In both cases, the correlation windows are overlapped as per estimate.

It should be noted that the coherence estimate suffers from significant bias and poor STD for small number of independent samples in combination with low coherence [34, 35]. This leads to a practical lower estimation level (or bias floor) that is non-zero for completely uncorrelated signals.

Figure 6 shows the estimates of SAS and SSS coherence of an example 50×360 m flat seabed with trawl marks. The two left panels are with 15 m altitude and the two right panels with 90 m altitude. Clearly, the nadir blindzone increases with altitude, but so does also the maximum valid ground range. The figure shows that SSS and SAS coherence are very similar, confirming that the synthetic aperture synthesis only changes resolution, not SNR. The difference at long range for 15 m altitude is due to the longer range correlation window for SSS, and different lower bias floor due to different number of independent samples.

The figure also shows the strong dependence between coherence (and thus SNR) and grazing angle. This can be most easily seen in the second panel from the left, where there is high variability in the coherence everywhere the trawl marks cause changes in the grazing angle.

3.3 | Model fit

To better fit the model (1) to the measured SNR, we have added the following terms to the signal part: The maximum SNR is thresholded (softly)

$$\rho = (\rho^{-1} + \rho_{\max}^{-1})^{-1} \quad (15)$$

where ρ_{\max} is the practical maximum achievable SNR. The reason for this thresholding is that there are various sources of

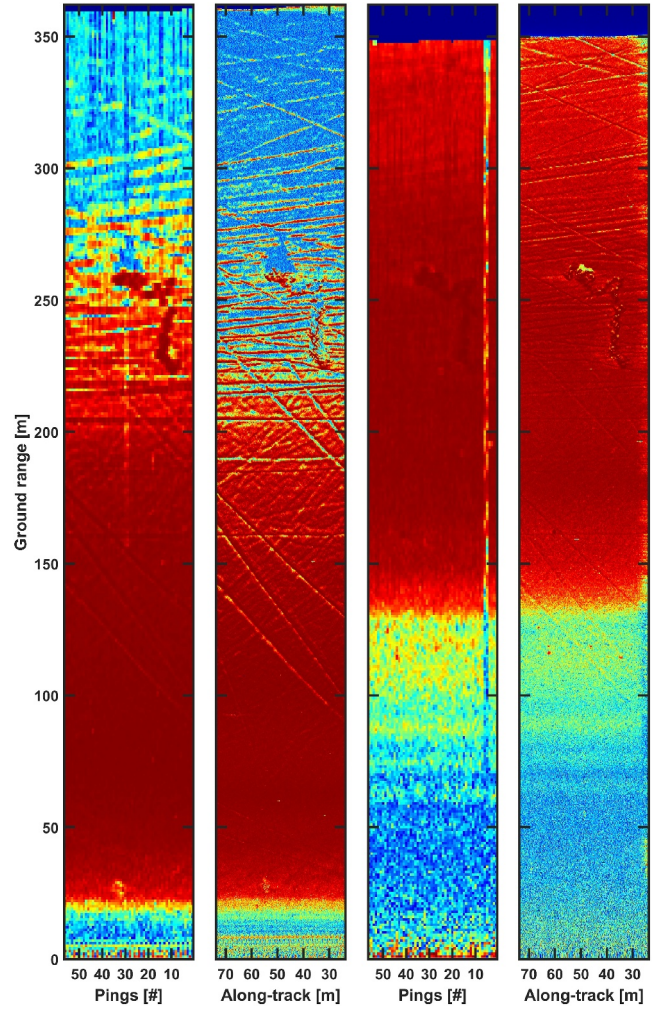


FIGURE 6 Coherence estimates for a 50×360 m scene. Left to right: SSS coherence with $h = 15$ m, SAS coherence with $h = 15$ m, SSS coherence with $h = 90$ m and SAS coherence with $h = 90$ m. The stripe with coherence loss in the SSS coherence with $h = 90$ m is due to acoustic interference. The dynamic range is from 0 (blue) to 1 (red).

decorrelation in addition to additive noise [9] that in effect limit the coherence. In addition, we moderate the modelled SNR (or rather the modelled coherence) as follows:

$$\bar{\gamma}(r) = \gamma(r)e^{-\alpha(r)}, \quad \alpha(r) = \alpha_0 \left| \frac{\partial \phi_g(r)}{\partial r} \right| \quad (16)$$

where $\alpha_0 > 0$ is a suitable scaling factor. This correction lowers the coherence values when approaching nadir. Correspondingly, the correction approaches one (no correction) when the grazing angle approaches zero. This behaviour is similar to the geometry induced time-stretching error that increases the more vertical the imaging geometry is [10, 35].

The algorithm to fit the model (1) to the measurements can then be summarised as:

1. Assume a seabed type, system setup, and geometry.
2. Use the modified grazing angle (4) to calculate the back-scattering coefficient.

3. Calculate the predicted signal level.
4. Choose a suitable noise level N_0 to fit observations at far range.
5. Soft-threshold the modelled SNR (15) and fit the peak to observations.
6. Add the coherence-reduction term due to grazing angle changes at near range (16).

Figure 7 shows the estimated SNR from SSS coherence (solid lines) compared with the model fit (dotted lines) for the six different altitudes. The measurements are based on 1000 pings from the forward lines and 1000 pings from the return lines, median filtered and averaged. The seabed in the area covered is fairly flat, except for small perturbations in depth caused by trawl marks. We see good agreement between the model and the measurement over the entire range span, and for all altitudes. There are some small differences between port and starboard measurements that may be explained by vehicle roll and pitch, and differences in the beampatterns. Note that the measured SNR at 15 m altitude at maximum range flattens out due to the bias floor in the coherence estimator [35]. There are other small variations that could be explained from the fact that the scene is non-flat. In general the model is however a good fit of the measurements and captures the essential behaviour, which confirms that the proposed model can be successfully used to predict the performance of the sonar as function of range.

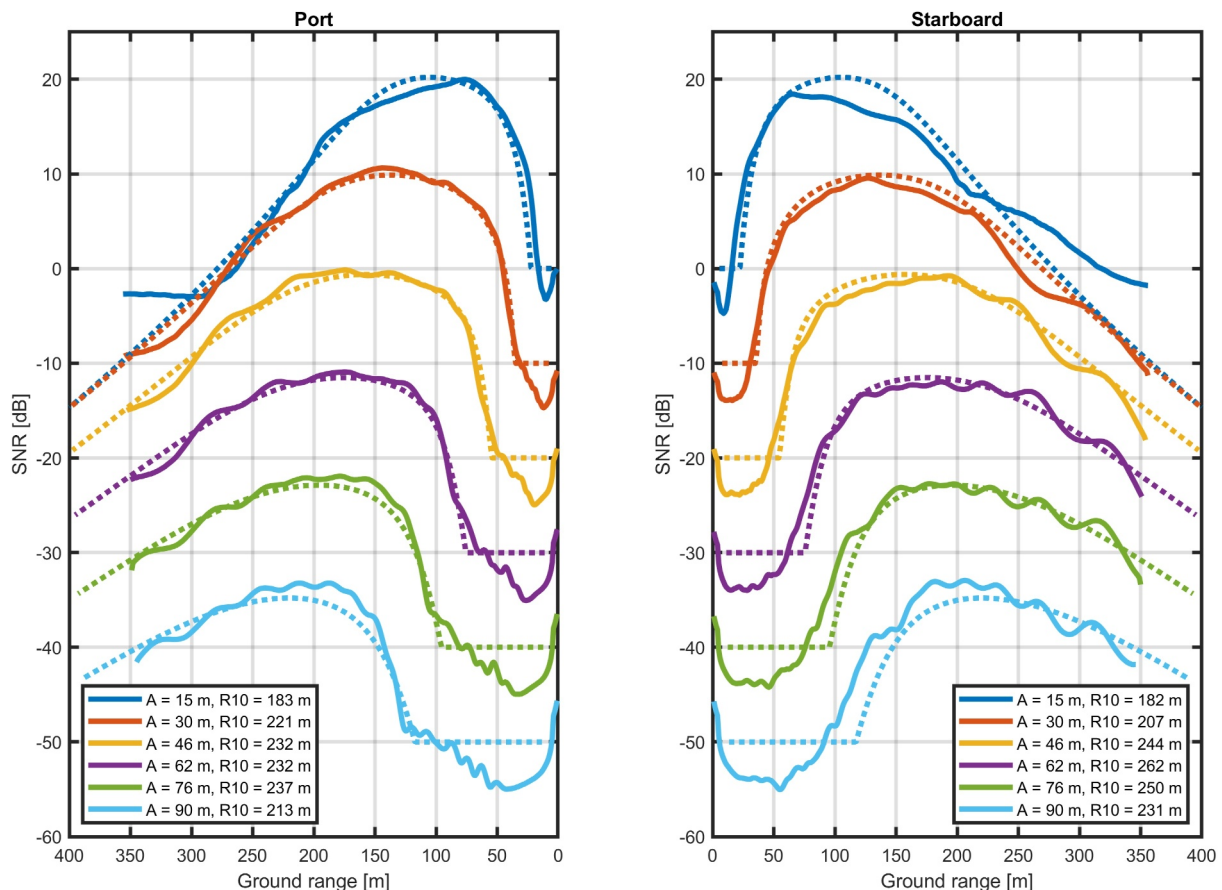


FIGURE 7 Estimated SSS SNR (solid lines) compared with the model fit (dotted lines) for six different altitudes (different colours). The result from each altitude from 30 m and upwards are shifted -10 dB per step to improve readability. Bottom type Medium silt is used in the model.

3.4 | Performance criterion

The achievable swath and effective area coverage rate is a function of how we choose the performance criterion. A common criterion in SAS imaging is that the area must be covered (visible in the sonar image) and that the geometry (the grazing angle) is within bounds. A better criterion for SAS interferometry is to define the achievable swath by requiring the interferometric coherence to be above some given threshold. Or equivalently, the SNR must be above some threshold. This is a sensible choice, since interferometry processing techniques require a certain SNR to function properly.

If we choose R_{\max} as the 10 dB crossing at long range and R_{\min} as the 10 dB crossing at short range in Figure 7, we can study the swath width $R_{\text{swath}} = R_{\max} - R_{\min}$ as function of altitude. Figure 8 shows R_{swath} for both the measurements and the model. The figure also shows the nadir gap $2R_{\min}$. We see that the model fits the measurements well. Our results show that the swath width is largest for an altitude of around 60 m. At lower altitudes, there is insufficient SNR at long range, and at higher altitudes, the blind zone increases while the attenuation lowers the long range SNR. So for this experiment, 60 m altitude would provide the largest area coverage rate. It should be noted that if we choose a more sensible 3 dB criterion for the achievable swath, our R_{\max} results would be limited by the recording slant-range of 370 m, and not the SNR being below the threshold for the high altitude cases.

From Figure 8, it is clear that our fitted model in Equation (1) gives us a possibility to numerically optimise the effective area coverage rate.

A potentially better optimisation criterion is to define the minimum and maximum range giving a depth STD (8) below some threshold. Figure 9 shows the theoretical STD for the six different altitudes when using the calibrated model. We have chosen a SAS setup with 0.5×0.5 m correlation window with approximately 500 independent pixels at maximum range. The modelled accuracy is unrealistically low at minimum value due to the unrealistically high modelled SNR. Note the non-linear varying nature of this quality metric. From Equation (8), we see that

$$\sigma_z \sim R \frac{1}{\rho} \quad \text{when } \rho \gg 1, \quad (17)$$

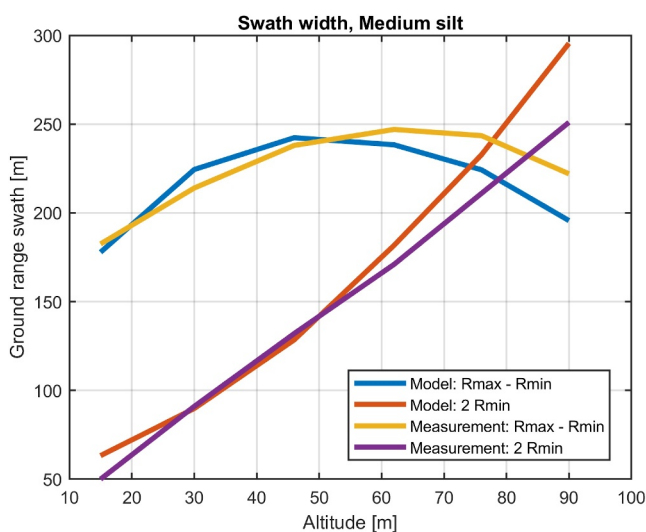


FIGURE 8 Modelled and measured ground range swath width.

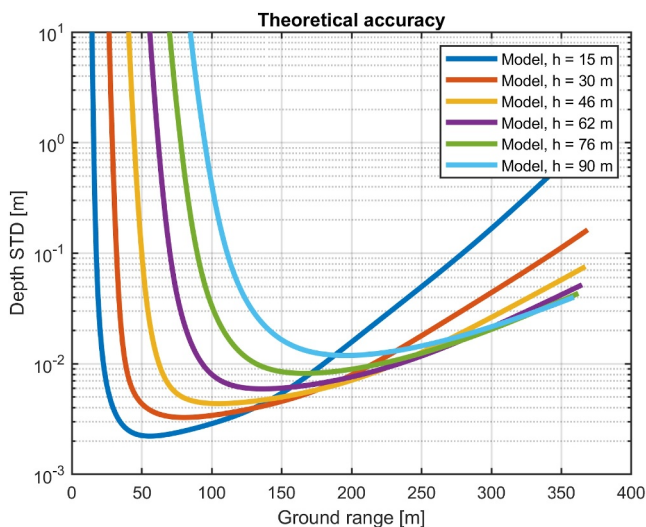


FIGURE 9 Modelled depth STD for different altitudes.

which indicates an explicit range dependence in combination with the SNR dependence. This penalises large ranges, with regard to performance. Figure 10 shows the modelled achievable swath (solid lines) for STD thresholding (blue) and SNR thresholding (red). We have chosen a depth STD threshold such that the nadir gap $2R_{\min}$ fits the SNR thresholded results. We see a range penalty for the STD. The maximum swath is achieved at 50 m altitude for SNR thresholding, and 40 m altitude for STD thresholding.

Note that if the horizontal resolution for seabed mapping is allowed to change within the swath [13], this will affect the optimisation, and potentially a different collection geometry will give the best performance. The methodology and approach can still be used.

3.5 | Coverage within swath

To better visualise the SAS seabed mapping performance of this system as a function of altitude, we have selected a 35×50 m scene with trawl marks and a rock formation. Figure 11 shows the SAS image of the scene. The rock formation is at 245 m ground range. Figure 12 shows the estimated coherence and the estimated depth maps for the six different altitudes. We see that the three lowest altitudes provide inferior depth maps relative to the three highest altitudes. Note also the relatively large fraction of the scene not being mapped due to the coherence being below a threshold, especially for the lowest altitude. The fraction covered inside the scene, or *coverage within swath*, could also be formed into a performance criterion, similar to the average SNR or the average depth STD. Note that this performance metric is a function of the terrain variations in the scene.

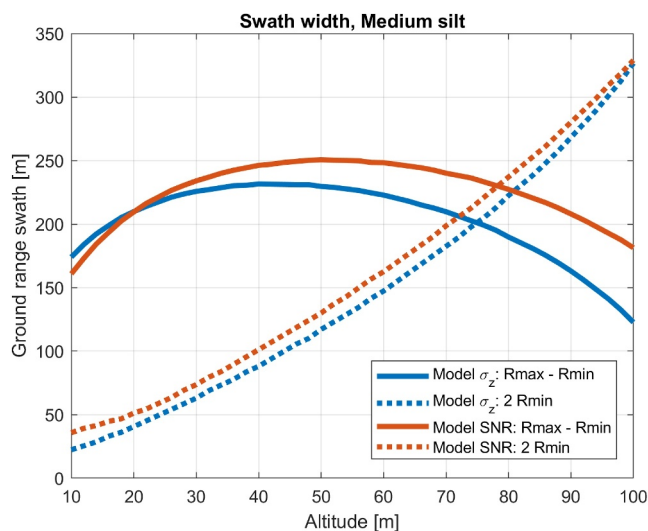


FIGURE 10 Modelled swath width. Blue: SNR limited. Red: STD limited. The STD threshold is tuned to get approximately equal minimum range.

3.6 | Optimisation procedure

To summarise, we suggest the following procedure for optimising collection geometry for seabed mapping using interferometric SAS:

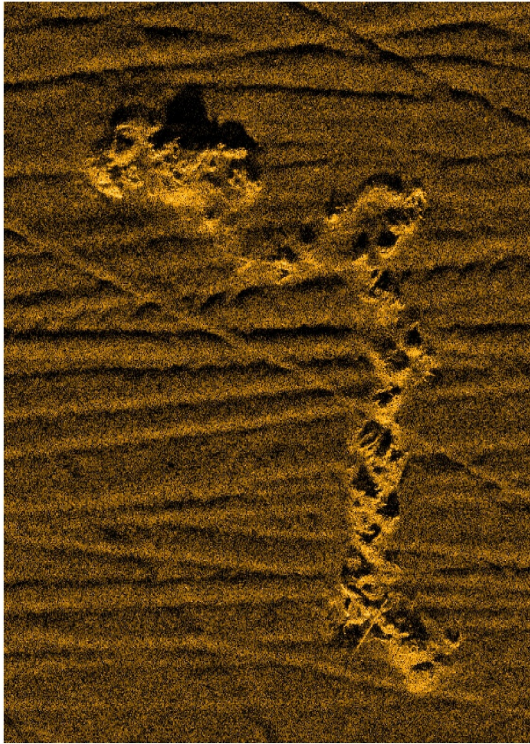


FIGURE 11 SAS image of the rock formation. The size of the image is 35×50 m, the range to the centre of the scene is 245 m and the dynamic range is 50 dB. The vehicle altitude was 60 m, and the port side sonar was used to produce this image. The theoretical resolution in the image is 3×3 cm.

Data collection Collect reference data for calibration of the model. The scene should ideally be homogeneous and flat.

Processing Calculate average coherence and SNR as function of geometry and range.

Model calibration Choose a seafloor type, and sonar settings for the given geometry. Fine-tune the free parameters to calibrate the model.

Performance criteria Choose a set of performance criteria based on nominal imaging geometry, SNR above some threshold, depth STD below some threshold, and coverage within swath.

Optimise geometry Run the calibrated model to calculate the achievable swath given the criteria multiple iterations using different collection geometries, for example, vehicle altitude. Then choose the collection geometry that maximises the effective area coverage rate.

Production Run data collection with the optimised collection geometry for production of seabed maps.

Adaptation Measure through-the-sensor overall performance in the collected data. Rerun the calibrated model. Adjust the collection geometry to maximise performance.

The adaptation-stage is well suited to run fully automated during production.

The same optimisation procedure can also be used to optimise other parameters such as vertical beampattern, pulse length, centre frequency and bandwidth.

4 | CONCLUSION

In this paper, we have studied the performance of long-range SAS interferometry for seabed mapping. For long range systems, traditional geometry provides very small grazing angles at

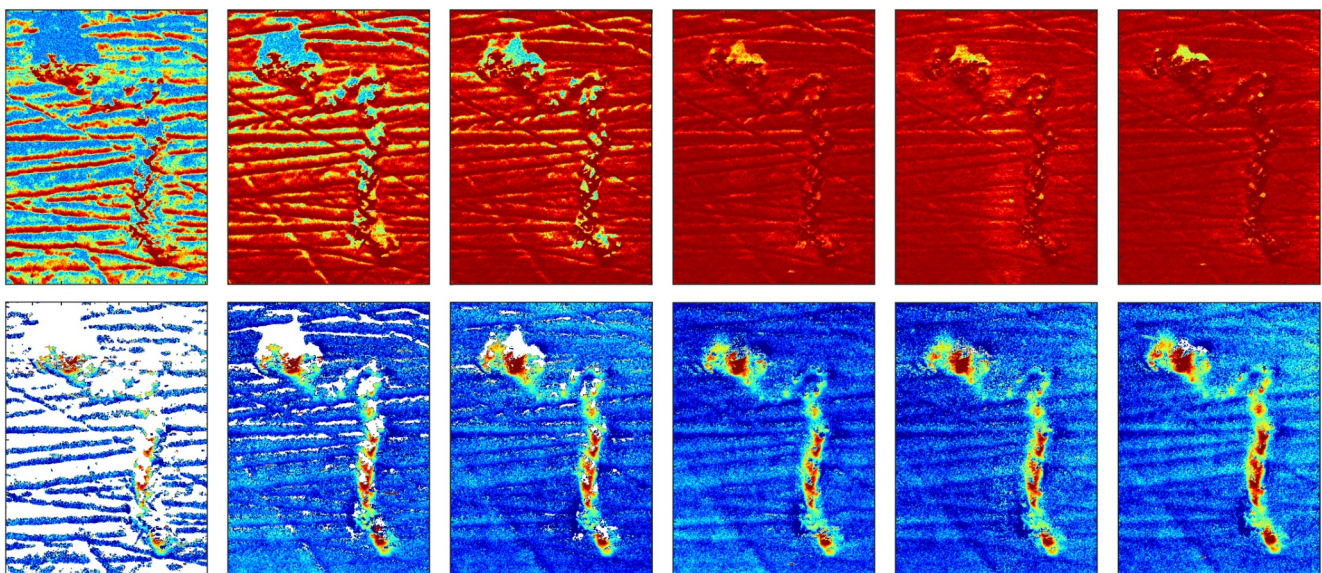


FIGURE 12 Coherence (upper) and estimated bathymetry (lower) for a 35×50 m scene with flat seabed and a rock formation. The dynamic range is from 0 (blue) to 1 (red) in the coherence plots and with 1 m depth variation in the bathymetry plots. Left to right: Altitude equal to 15, 30, 45, 60, 75 and 90 m. The data are from starboard side.

maximum range, which may lead to insufficient SNR for accurate seabed mapping. Equivalently, increasing the altitude increases the nadir blind zone and also increases the range dependent attenuation and energy spreading loss.

We have suggested a simplified model to predict the SNR and thus also the variance of the interferometric estimates. We have compared this model to experimental data using a HISAS 1032 Dual Rx system and found that the model relatively accurately describes the minimum and maximum valid mapping range.

We have also described the relationship between the minimum and maximum range and the effective area coverage rate, when the SAS sensor covers its own blind zone in a lawnmower pattern.

Finally, we have presented a direct procedure for optimising the collection geometry for long range seabed mapping that is well suited for fully automated processing. This procedure is also suitable for optimising other sonar parameters such as vertical beampatterns and pulse parameters.

AUTHOR CONTRIBUTIONS

Roy Edgar Hansen: Conceptualization; Formal analysis; Methodology; Writing – review & editing. **Torstein Olsmo Sæbø:** Conceptualization; Data curation; Formal analysis; Methodology; Writing – original draft.

ACKNOWLEDGEMENTS

The authors thank Darrel Jackson from Applied Physics Laboratory at University of Washington, Seattle, for providing code to produce the sediment backscatter model used in this study. The authors also thank Anthony Lyons from Center for Coastal and Ocean Mapping/Joint Hydrographic Center at University of New Hampshire for valuable discussions on seabed backscatter. The authors also thank the colleagues at FFI: Ole Lorentzen, Marc Geilhufe, and Stig Synnes. Finally, the authors thank Kongsberg Discovery for providing data for the study.



CONFLICT OF INTEREST STATEMENT

The authors have no conflict of interest.

DATA AVAILABILITY STATEMENT

Research data are not shared.

ORCID

Roy Edgar Hansen  <https://orcid.org/0000-0003-3111-1259>
Torstein Olsmo Sæbø  <https://orcid.org/0000-0002-8886-8538>

REFERENCES

- Griffiths, H.D., et al.: Interferometric synthetic aperture sonar for high-resolution 3D mapping of the seabed. *IEE Proc. Radar, Sonar Navig.* 144(2), 96–103 (1997). <https://doi.org/10.1049/ip-rsn:19971076>
- Rosen, P.A., et al.: Synthetic aperture radar interferometry. *Proc. IEEE* 88(3), 333–382 (2000). <https://doi.org/10.1109/5.838084>
- Bamler, R., Hartl, P.: Synthetic aperture radar interferometry. *Inverse Probl.* 14(4), R1–R54 (1998). <https://doi.org/10.1088/0266-5611/14/4/001>
- Hagen, P.E., Hansen, R.E.: Area coverage rate for synthetic aperture sonars. In: *Proceedings of Oceans '07 Europe*. Aberdeen, Scotland (2007). <https://doi.org/10.1109/OCEANSE.2007.4302382>
- Cutrona, L.J.: Comparison of sonar system performance achievable using synthetic-aperture techniques with the performance achievable by more conventional means. *J. Acoust. Soc. Am.* 58(2), 336–348 (1975). <https://doi.org/10.1121/1.380678>
- Hansen, R.E.: Introduction to synthetic aperture sonar. In: Kolev, N.Z. (ed.) *Sonar Systems*, pp. 3–28. Intech (2011). chapter 1. <https://doi.org/10.5772/23122>
- Sparr, T.: SAR and SAS compared - Equalities, similarities and differences. In: *Proceedings of Synthetic Aperture Sonar and Radar 2006* (2006)
- Sæbø, T.O., Hansen, R.E.: Comparison between interferometric SAS and interferometric SAR. In: *Proceedings of Synthetic Aperture Sonar and Radar 2010* (2010)
- Hanssen, R.F.: *Radar Interferometry: Data Interpretation and Error Analysis*. Kluwer Academic Publishers, Dordrecht (2001)
- Sæbø, T.O.: *Seafloor Depth Estimation by Means of Interferometric Synthetic Aperture Sonar*. PhD thesis. University of Tromsø, Norway (2010)
- Sæbø, T.O., Synnes, S.A.V., Hansen, R.E.: Wideband interferometry in synthetic aperture sonar. *IEEE Trans. Geosci. Rem. Sens.* 51(8), 4450–4459 (2013). <https://doi.org/10.1109/tgrs.2013.2244900>
- Sæbø, T.O., Hansen, R.E., Synnes, S.A.V.: Phase ambiguities in synthetic aperture sonar interferometry. In: *Proceedings of Oceans 2022 MTS/IEEE* (2022). <https://doi.org/10.1109/OCEANS47191.2022.9977342>
- Sæbø, T.O., Hansen, R.E.: Adaptive phase estimation filter in long range synthetic aperture sonar interferometry. *Electron. Lett.* 59(10), e12819 (2023). <https://doi.org/10.1049/ell2.12819>
- Sæbø, T.O., Hansen, R.E., Lorentzen, O.J.: Long-range interferometric synthetic aperture sonar. In: *Proceedings of Synthetic Aperture Sonar and Synthetic Aperture Radar 2023* (2023)
- Mills, R., et al.: Addressing the need to grow AUV operator workforce: advanced autonomy and goal based mission planning. In: *OCEANS 2023 - MTS/IEEE U.S. Gulf Coast*, pp. 1–6 (2023). <https://doi.org/10.23919/OCEANS52994.2023.10337110>
- Hagen, P.E., et al.: An integrated, scalable, SAS based system for acoustic imaging and bathymetry. In: *OCEANS 2018 MTS/IEEE Charleston* (2018). <https://doi.org/10.1109/OCEANS.2018.8604571>
- Lurton, X.: *An Introduction to Underwater Acoustics: Principles and Applications*, 2nd ed. Springer Praxis Publishing, London (2010)
- Ainslie, M.A.: *Principles of Sonar Performance Modelling*. Springer Verlag (2010)
- Richards, M.A., Scheer, J.A., Holm, W.A.: *Principles of Modern Radar. Basic principles* (2010)
- Richards, M.A.: *Fundamentals of Radar Signal Processing*, 2nd ed. McGraw-Hill Book Company (2014)
- Cook, D.A., Brown, D.C.: Synthetic aperture sonar image contrast prediction. *IEEE J. Ocean. Eng.* 43(2), 523–535 (2018). <https://doi.org/10.1109/joe.2017.2702843>
- Lyons, A.P., Olson, D.R., Hansen, R.E.: Modeling the effect of random roughness on synthetic aperture sonar image statistics. *J. Acoust. Soc. Am.* 152(3), 1363–1374 (2022). <https://doi.org/10.1121/10.0013837>
- Massonnet, D., Souyris, J.C.: *Imaging with Synthetic Aperture Radar*. Engineering sciences. EFPL Press, Lausanne (2008)
- Jackson, D.R., Richardson, M.D.: *High Frequency Seafloor Acoustics*. Springer (2007)
- Richardson, M.D., Jackson, D.R.: The seafloor. In: Bjørnø, L., Neighbors, T., Bradley, D. (eds.) *Applied Underwater Acoustics*, pp. 469–552. Elsevier (2017). chapter 8
- APLUW94: *High-frequency Ocean Environment Acoustic Models Handbook*. Technical Report APL-UW TR 9407. Applied Physics Laboratory, University of Washington (1994)
- Del Balzo, D.R., Leclere, J.H., Collins, M.J.: Critical angle and seabed scattering issues for active-sonar performance predictions in shallow

- water. In: High Frequency Acoustics in Shallow Water, SAACLANTCEN Conference Proceedings Series CP- 45. Nato Saclantcen (1997)
28. Quazi, A.H.: An overview on the time delay estimate in active and passive systems for target localization. *IEEE Trans. Acoust. Speech Signal Process.*(3), 533–537 (1981). <https://doi.org/10.1109/TASSP.1981.1163618>
 29. Zebker, H.A., Villasenor, J.: Decorrelation in interferometric radar echoes. *IEEE Trans. Geosci. Rem. Sens.* 30(5), 950–959 (1992). <https://doi.org/10.1109/36.175330>
 30. Fish, J.P., Carr, H.A.: *Sound Reflections: Advanced Applications of Side Scan Sonar*. LowerCape Publishing (2001)
 31. Blondel, P.: *The Handbook of Sidescan Sonar*. Geophysical Sciences. Springer Praxis Books (2009)
 32. Burguera, A., Oliver, G.: High-resolution underwater mapping using side-scan sonar. *PLoS One* 11(1), 1–41 (2016). <https://doi.org/10.1371/journal.pone.0146396>
 33. Hoggarth, A., Kenny, K.: Using synthetic aperture sonar as an effective hydrographic survey tool. In: 2014 Oceans, pp. 1–12. IEEE, Canada (2014). St. John's, NL. <https://doi.org/10.1109/OCEANS.2014.7003108>
 34. Touzi, R., et al.: Coherence estimation for SAR imagery. *IEEE Trans. Geosci. Rem. Sens.* 37(1), 135–149 (1999). <https://doi.org/10.1109/36.739146>
 35. Synnes, S.A.V., Hansen, R.E., Sæbø, T.O.: Spatial coherence of speckle for repeat-pass synthetic aperture sonar micronavigation. *IEEE J. Ocean. Eng. 46(4)*, 1330–1345 (2021). <https://doi.org/10.1109/joe.2021.3060812>

How to cite this article: Hansen, R.E., Sæbø, T.O.: Optimising collection geometry for long-range synthetic aperture sonar interferometry. *IET Radar Sonar Navig.* 1–10 (2024). <https://doi.org/10.1049/rsn2.12607>